Highlights

A Finite Volume Based Fully Nonlinear Potential Flow Model for Water Wave Problems

Zaibin Lin, Ling Qian, Wei Bai, Zhihua Ma, Hao Chen, Jian-Guo Zhou, Hanbin Gu

- A new fully nonlinear potential flow wave model based on Finite Volume Method
- A new Fourth-Order Damping Correction scheme is proposed and implemented
- The model is validated against existing numerical and experimental results
- It provides an alternative for coupling with multiphase flow solvers in OpenFOAM

A Finite Volume Based Fully Nonlinear Potential Flow Model for Water Wave Problems

Zaibin Lin[a], Ling Qian[a,*], Wei Bai[a], Zhihua Ma[a], Hao Chen[b], Jian-Guo Zhou[a], Hanbin Gu[c]

[a] *Centre for Mathematical Modelling and Flow Analysis, Department of Computing and Mathematics, Manchester Metropolitan University, Manchester, M1 5GD, United Kingdom*

[b] *School of Engineering, University of Glasgow, Glasgow G12 8QQ, United Kingdom*

[c] *Research Institute of Ocean Engineering, Ningbo University, Ningbo, Zhejiang, China*

Abstract

A new Fully Nonlinear Potential Flow (FNPF) numerical model has been developed for the simulation of nonlinear water wave problems. At each time step, the mixed boundary value problem for the flow field is spatially discretised by Finite Volume Method (FVM) and the kinematic and dynamic free surface boundary conditions are defined in a semi-Eulerian-Lagrangian form, which are used to update the wave elevation and velocity potential on the free surface. In the numerical model, waves are generated through a relaxation zone and absorbed by an artificial damping zone at the inlet and outlet of the numerical wave tank (NWT), respectively. Instead of a five-point smoothing technique, a more versatile fourth-order technique is developed to eliminate the possible saw-tooth instability at the free surfaces. Test cases of increasing complexities, such as wave generation and absorption, 2- and 3-Dimensional wave shoaling, and wave-cylinder interaction are simulated to assess its accuracy, convergence, and robustness. For all the cases considered, satisfactory agreements of free surface elevation and wave-induced forces against the experimental measurements and other existing numerical results are achieved. The developed numerical model fully utilises the existing functionalities in OpenFOAM and has the potential to provide an effective alternative to other FNPF based models for constructing a hybrid numerical wave tank model through its coupling with the multiphase flow models in OpenFOAM.

Keywords:
Fully nonlinear potential flow, Finite volume method, OpenFOAM, Wave

*Corresponding author
Email address: l.qian@mmu.ac.uk (Ling Qian)

shoaling, Wave-structure interaction

1. Introduction

As a challenging and longstanding scientific problem in coastal, ocean, and offshore engineering, the development of an accurate, efficient, and robust numerical model for wave-wave and wave-structure interactions has been the ultimate goal of computational hydrodynamics. For non-breaking water waves propagation and transformation in the areas from deep offshore water to shallow water, Fully Nonlinear Potential Flow (FNPF) numerical models can provide sufficiently accurate solutions to practical engineering problems.

In the past decades, substantial progress has been made in applying the fully nonlinear potential flow theory for wave-wave and wave-structure interactions. Various conventional discretisation methods, such as Boundary Element Method (BEM), Finite Element Method (FEM), and Finite Difference Method (FDM), have been adopted to provide accurate solutions to potential flow problems. Whilst FDM (Bingham and Zhang, 2007; Engsig-Karup et al., 2009) as used in OceanWave3D and FEM (Wu and Eatock Taylor, 1994; Wu et al., 1998) solve a sparse linear equation system resulting from the discretisation of full computational domain, BEM requires the representation of boundaries including free surfaces only, leading to the formulation of the boundary integral equation in association with the Green's function and the formation of a full asymmetric matrix (Celebl et al., 1998; Bai and Eatock Taylor, 2006; Eatock Taylor et al., 2008; Bai and Eatock Taylor, 2009; Bai et al., 2014; Hannan and Bai, 2015; Ning et al., 2015). By extending a 2-Dimensional (2-D) FNPF model (Grilli et al., 1989), Grilli et al. (2001) further developed a 3-Dimensional (3-D) FNPF model based on higher-order BEM. It was demonstrated that the high-resolution regridding approach used in the 3-D BEM FNPF model can be applied to simulate the highly nonlinear process of overturning breaking waves (Guyenne and Grilli, 2006). In order to improve the efficiency of this 3-D FNPF model, Fochesato and Dias (2006) incorporated the Fast Multipole Algorithm (FMA) to substitute matrix-vector product operations and prevent the formation of influence matrix. By reducing computational complexity from O(N^2) to nearly O(N), this 3-D BEM based FNPF model with FMA considerably improved computational efficiency of the higher-order 3-D BEM FNPF model and allows

for large-scale parallel computing. In the meantime, further improvements to the FEM based solvers have also been made. Ma et al. (2001a,b) implemented an extrapolation scheme for boundary cells to improve the FEM solution and applied the model to investigate the interactions between waves and a fixed cylinder. The FEM FNPF model was further extended using the Quasi Arbitrary Lagrangian-Eulerian approach (QALE-FEM) (Ma and Yan, 2006), which adopts unstructured mesh and avoids mesh regeneration at every time step. The developed code was applied to investigate 2-D (Yan and Ma, 2007) and 3-D (Ma and Yan, 2009) wave interaction with floating structures, demonstrating its capability in accurately capturing 6 Degree of Freedom of body motions.

In addition to the conventional discretisation methods, several alternative efficient or high-order discretisation methods have been proposed with less spatial representations, such as Harmonic Polynomial Cell (HPC) in Shao and Faltinsen (2014), Spectral Element Method (SEM) in Engsig-Karup et al. (2016) and Engsig-Karup and Eskilsson (2019), High-Order Spectral (HOS) model in Ducrozet et al. (2006) and Ducrozet et al. (2016), and spectral boundary integral method in Wang and Ma (2015) and Wang et al. (2016). The σ-coordinate transformation is another commonly applied technique to deal with the change of the computational domain due to the movement of free surfaces, which has been implemented in FEM, FDM, and SEM in Cai et al. (1998),Turnbull et al. (2003), (Bingham and Zhang, 2007), and Engsig-Karup et al. (2009, 2012, 2016). An extensive comparative study of high-order FDM and pseudo-spectral HOS method Ducrozet et al. (2006) demonstrated that given the same level of solution accuracy the pseudo-spectral HOS method presents better computational efficiency for cases of long-distance wave propagation. Although high computational efficiency can be achieved using σ-coordinate transformation, one potential difficulty associated with the method lies in the handling of the potentially complex geometry when simulating wave interaction with floating structures. To overcome this, an overlapping body fitted mesh was introduced in Amini-Afshar et al. and the concept is rather similar to the overset meshing technique (Chen et al., 2019b). As the majority of work on the FNPF models was based on the Mixed-Eulerian-Lagrangian (MEL) method or semi-Eulerian-Lagrangian method, in which the mesh is updated at every time step, another feasible solution to deal with the interaction between waves and semi-submersible or fully submerged floating structures is to develop FNPF models based on

MEL with aforementioned high-order discretisation method (Engsig-Karup et al., 2019; Engsig-Karup and Eskilsson, 2019).

It is well known that the FNPF models fail to correctly simulate post-wave breaking flows and violent wave impact on structures where the effects of fluid viscosity including flow turbulence may become important, although it is possible to apply them to model initial wave overturning process (Grilli et al., 2001; Yan and Ma, 2010; Song and Zhang, 2018). On the other hand, the open source package OpenFOAM, which is based on the NS-VoF models and capable of modelling complex wave structure interaction problems, has become increasingly popular. Wave generation and absorption techniques, such as Jacobsen et al. (2012), Higuera et al. (2013, 2015), Martínez-Ferrer et al. (2018), and Chen et al. (2019a), have been integrated into the *interFoam* solver in OpenFOAM and the models have been applied to simulate violent wave impact on ocean and coastal structures under extreme conditions (Paulsen et al., 2014b; Lin et al., 2016, 2017, 2020). However, compared to FNPF models, the computational costs of these solvers are still very high and inherent numerical damping in the solution may lead to energy loss in waves travelling over a long distance. This has led to the development of one-way or two-way coupled FNPF and NS-VoF models (Guignard et al., 1999; Paulsen et al., 2014a; Yan et al., 2019), as well as coupled FNPF and meshless/particle models (Sriram et al., 2014), with the premise that wave generation/propagation and wave/wave interactions over a large portion of the domain can be modelled by an efficient FNPF solver while the local complex fluid-structure interactions can be resolved by NS-VoF or meshless/particle models.

As FVM is the discretisation method adopted in OpenFOAM, the development of a 3-D FNPF numerical model based on FVM which can be coupled with NS-VoF solvers within the framework of OpenFOAM provides a number of advantages. For examples, all the advanced features and functionalities of OpenFOAM can be fully utilised when developing the new numerical model, including mesh generation, advanced discretisation schemes and OpenMPI for parallelisation. Furthermore, compared to other hybrid numerical wave tank models based on different numerical discretisation methods, programming languages and code development environments a FVM based FNPF free surface model can provide a seamless linkage to the existing NS-VoF models in OpenFOAM with the potential to achieve better code accuracy

and efficiency. Earlier work along this line e.g. Mehmood et al. (2015, 2016) has been focused on 2-D wave only problems and suffers from numerical instabilities for long time simulations. In the present work, a new 3-D FVM based FNPF free surface solver has been developed. This is achieved through implementing kinematic and dynamic boundary conditions at free surfaces and wave generation and absorption techniques based on linear and high order wave theories. To maintain the numerical stability of the solver a new smoothing technique applicable to both structured and unstructured meshes is proposed and implemented. A number of test cases have been used to validate the developed solver including wave generation and propagation in 3-D tanks, wave shoaling over 2-D and 3-D slopes, and wave interaction with a fixed cylinder, demonstrating its ability to accurately and efficiently capture highly nonlinear water waves and their interaction with structures. In the following sections, the mathematical formulation of the method is firstly outlined which is followed by the details of numerical implementation including both kinematic and dynamic boundary conditions using the semi-Eulerian-Lagrangian approach and Fourth-Order Damping Correction scheme to eliminate sawtooth instability. Then, the numerical solutions from the current solver for a number of test cases are presented and validated against existing numerical and experimental data. Finally, key conclusions from the present work are given along with a brief plan for the future work.

2. Mathematical formulation

Under the assumption that the fluid is incompressible, inviscid and flow irrotational, the potential flow theory is adopted here to simulate the fully nonlinear water waves. In a computational domain with a Cartesian coordinate system defined, still water surface is located in the xz-plane and the y-axis points vertically upwards, as shown in Figure 1. The governing equation is given as follow:

$$\nabla^2\phi = 0 \tag{1}$$

where ϕ is the velocity potential. To formulate the boundary value problem for water wave problems, the kinematic and dynamic boundary conditions are satisfied on free surface:

$$\frac{\partial \eta}{\partial t} = \frac{\partial \phi}{\partial y} - \frac{\partial \phi}{\partial x}\frac{\partial \eta}{\partial x} - \frac{\partial \phi}{\partial z}\frac{\partial \eta}{\partial z} \tag{2}$$

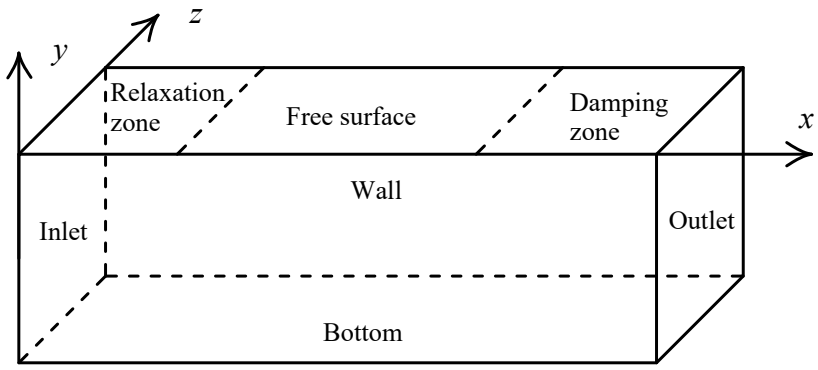

Figure 1: Sketch of the numerical wave flume.

$$\frac{\partial \phi}{\partial t} = -\boldsymbol{g}\eta - \frac{1}{2}\nabla\phi \cdot \nabla\phi \tag{3}$$

where η is wave elevation, $\boldsymbol{g}$ is gravitational acceleration, and t is the time. It should be noted that the boundary conditions in Eqs. (2) and (3) are presented in the Eulerian description. However, in the simulation of fully nonlinear wave problems, the free surface boundary conditions need to be satisfied on instantaneous moving boundary surface, leading to the introduction of the well-known Lagrangian description of the free surface boundary conditions. In present study, a semi-Lagrangian method is adopted, in which the total derivative $\frac{\delta(\ )}{\delta t}$ in the Lagrangian description is constructed by following a point on the free surface moving with a prescribed velocity $\boldsymbol{U_m}$,

$$\frac{\delta(\ )}{\delta t} = \frac{\partial(\ )}{\partial t} + \boldsymbol{U_m} \cdot \nabla(\ ) \tag{4}$$

When a point on the free surface is only allowed to move vertically, the prescribed velocity becomes $\boldsymbol{U_m} = (0, \frac{\partial \eta}{\partial t}, 0,)$. In addition, Eq. (2) is rewritten into an equivalent form in terms of the fluid particle velocity at the free surface $\boldsymbol{U}_\eta$ and the unit normal vector of the free surface $\boldsymbol{n}$ (Mayer et al., 1998), as they are readily available as part of the output at each time step in OpenFOAM. So, the fully nonlinear free surface boundary conditions in the semi-Lagrangian form can be expressed as follows:

$$\frac{\delta \eta}{\delta t} = \frac{\boldsymbol{U}_\eta \cdot \boldsymbol{n}}{n_y} \tag{5}$$

$$\frac{\partial \phi}{\partial t} = -\boldsymbol{g}\eta - \frac{1}{2}\nabla\phi \cdot \nabla\phi + \frac{\partial \eta}{\partial t}\frac{\partial \phi}{\partial y} \tag{6}$$

where n_y is the vertical component of the unit normal vector $\boldsymbol{n}$.

Furthermore, to avoid wave reflection a sponge layer is placed at the far end of a numerical wave flume. This is achieved by adding an additional term to the right-hand side of both the kinematic and dynamic boundary conditions to damp out the wave energy, and Eqs. (5) and (6) consequently become:

$$\frac{\delta \eta}{\delta t} = \frac{\boldsymbol{U}_\eta \cdot \boldsymbol{n}}{n_y} - v\left(x\right)\left(\eta - \eta_s\right) \tag{7}$$

$$\frac{\partial \phi}{\partial t} = -\boldsymbol{g}\eta - \frac{1}{2}\nabla\phi \cdot \nabla\phi + \frac{\partial \eta}{\partial t}\frac{\partial \phi}{\partial y} - v\left(x\right)\phi \tag{8}$$

$$v\left(x\right) = \begin{cases} \alpha\omega(\frac{x-x_0}{\beta\lambda})^2, & x \geq x_0 \\ 0, & x < x_0 \end{cases} \tag{9}$$

where x_0 is the starting point of the sponge layer; α and β are the damping coefficients that control the strength and length of the sponge layer, respectively; η_s is the at-rest free surface elevation; λ is the wavelength; and ω is the wave frequency. The length of sponge layer is recommended to be of 1-2 wavelengths (Ferrant, 1993; Bai and Eatock Taylor, 2006). At the other solid boundary surfaces of the computational domain, such as the side walls and the bottom, the impermeable condition is used. When the solid boundary is fixed, the boundary condition can be expressed as

$$\frac{\partial \phi}{\partial \boldsymbol{n}} = 0 \tag{10}$$

Once the velocity potential is determined by solving the boundary value problem, the pressure field of the entire domain can be predicted by the Bernoulli equation:

$$p = -\rho\left(\frac{\partial \phi}{\partial t} + \frac{1}{2}\nabla\phi \cdot \nabla\phi + \boldsymbol{g}y\right) \tag{11}$$

where ρ is water density. The corresponding hydrodynamic force on an object can then be obtained by the integration of pressure over its wetted

surfaces.

In present numerical wave flume, the waves are generated in the relaxation zone near the inlet boundary of the computational domain by the following equations:

$$\eta = \alpha_R \eta_{computed} + (1 - \alpha_R)\, \eta_{target} \tag{12}$$

$$\phi = \alpha_R \phi_{computed} + (1 - \alpha_R)\, \phi_{target} \tag{13}$$

where the subscripts *computed* and *target* represent the corresponding values from the computational results and the target waves respectively. This wave generation mechanism can also absorb the reflected wave from the structure inside a NWT, so as to avoid the unwanted second reflection from the inlet boundary. The relaxation function α_R is defined as (Bingham and Zhang, 2007; Jacobsen et al., 2012)

$$\alpha_R\left(\chi_R\right) = 1 - \frac{exp\left(\chi_R^{3.5}\right) - 1}{exp\left(1\right) - 1} \tag{14}$$

where χ_R is the function that satisfies $\chi_R = 0$ at the inlet and $\chi_R = 1$ at the end of a relaxation zone. It is suggested in Bingham and Zhang (2007) and Engsig-Karup (2007) that a relaxation zone of two wavelengths is able to sufficiently absorb the reflected wave. In this study, due to the use of a sponge layer at the far end of the wave tank, this relaxation zone is only located at the wave generation zone to generate waves and absorb possible reflected waves. From Eqs. (12) and (13), it can been seen that the values of wave elevation and velocity potential at the inlet boundary are determined by the corresponding values of the target waves and these will in turn drive the generation of waves in the computational domain. Due to this, the solid wall or zero-flux condition (Eq.(10)) is applied at both inlet and outlet boundaries when solving the Laplace equation (Eq. (1)

3. Numerical implementation

As indicated above, the present numerical wave flume is developed on the platform of the software package OpenFOAM and the existing functions/modules, e.g. the Laplacian solver in OpenFOAM, are fully utilised to avoid duplication of work. To solve the Laplace equation (Eq.1), it is first

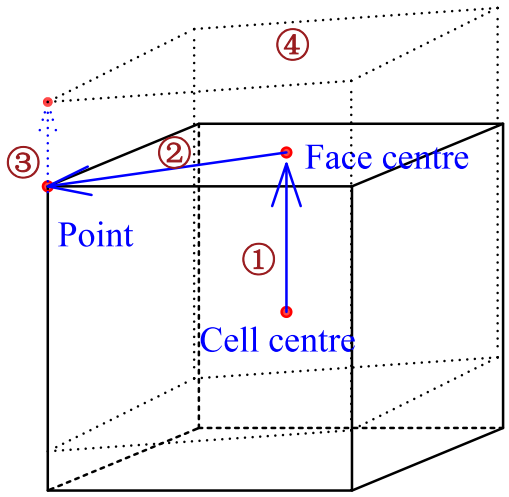

Figure 2: Interpolation and mesh update process on a mesh cell on free surface.

integrated over a computational cell of volume V and then converted into surface integration based on Gauss theorem, which in turn is discretised into the sum of the dot product from all cell face values:

$$\int_V \nabla \cdot (\nabla\phi)\, dV = \oint_S \nabla\phi \cdot d\vec{S} = \sum_i^{\text{nFace}} (\nabla\phi)_{f,i} \cdot \vec{S}_{f,i} = 0 \tag{15}$$

where $\vec{S}_{f,i} = A_{f,i}\vec{n}_{f,i}$, $A_{f,i}$ and $\vec{n}_{f,i}$ are the area and outward unit normal of cell face i respectively.

In present numerical model, computational mesh needs to be updated every time step to account for the motion of free surfaces. This is done by stretching the mesh in the vertical direction using the semi-Lagrangian approach, as demonstrated in Figures 2 and 3. In OpenFOAM, the values of variables, such as velocity potential, pressure, and velocity field, are stored at cell centres, while the mesh update is based on cell vertices. This difference indicates the requirement of additional interpolations from cell centres to cell vertices in order to update the computational mesh according to the kinematic free surface boundary condition. The data interpolation and mesh update processes are shown in Figure 2. Firstly, the Laplace equation is solved numerically using the $fvm :: laplacian$ solver in OpenFOAM, in which a non-orthogonal correction scheme is applied to minimise the dis-

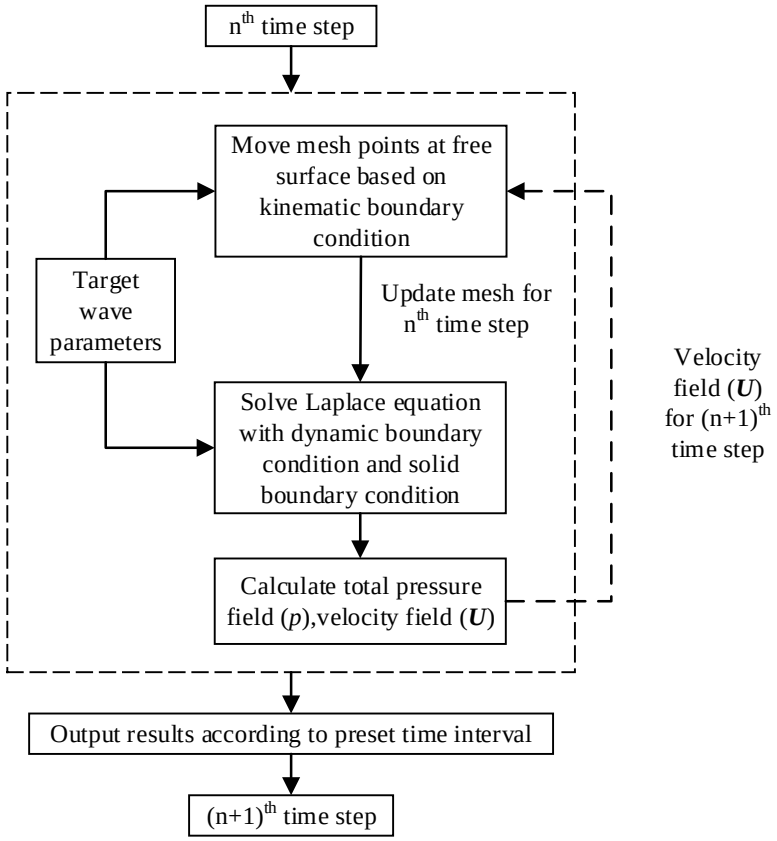

Figure 3: Interpolation and mesh update process on a mesh cell on free surface.

cretisation errors caused by mesh distortion, and the corresponding results are stored at cell centres. Secondly, the data at face centres on free surface are extrapolated from adjacent cell centres, as indicated by the first step in Figure 2. Then the data at neighbouring face centres are adopted to obtain the data at cell vertices on free surface by the distance-weighted interpolation indicated as the second step in Figure 2. After obtaining point field data from neighbour face centres, the cell vertices on free surface move vertically on the basis of the kinematic free surface boundary condition (see the third step in Figure 2). Finally, a fourth step is needed to update the mesh of the fluid domain based on the updated positions of cell vertices on free surfaces from the third step.

The overall flow chart for the solution of the fully nonlinear potential flow model for water wave problems is shown in Figure 3. In additional to the mesh update process in Figure 2, the first-order Euler explicit time scheme is used to discretise the unsteady term in the free surface boundary conditions and update the wave elevation (Eqs. 5 and 7) and velocity potential (Eqs. 6 and 8) on the free surface respectively. By introducing target wave parameters into the relaxation zone (Eqs. 12-14) in the kinematic and dynamic boundary conditions, the Laplace equation is numerically solved using the new mesh updated by kinematic boundary condition from previous time step, together with solid boundary condition. After solving Laplace equation, velocity field ($\boldsymbol{U}$) is obtained for updating the mesh in next time step, together with pressure calculation based on Bernoulli equation (Eq. 11). During the simulation in the time domain, the time interval Δt between each step is determined by the Courant–Friedrichs–Lewy (CFL) condition where the CFL number is defined as $u\Delta t/\Delta x$, where u is the local typical velocity and Δx is the local typical mesh size. In present study, the CFL number is chosen to be 0.3 for all the cases.

One issue with the fully nonlinear potential flow model is the numerical instability, which has been reported and treated extensively in literature. This is due to the fact that any numerical error in the fully nonlinear potential flow model can be accumulated until it may build up the saw-tooth instability in many situations, as there is no energy dissipation under the potential flow assumption. As a general solution to deal with this numerical instability, the 5-point low-pass filter is used to smooth the wave elevation and velocity potential at the free surface boundary (Bai and Eatock Taylor, 2006, 2007; Shao and Faltinsen, 2014; Lin et al., 2019). Alternatively, the mesh regeneration and interpolation are another means to mitigate the numerical instability. In the present study, a new Fourth-Order Damping Correction (FODC) scheme is developed to work with the unstructured meshes at the free surface, which are introduced to better represent complex geometry of structures. In the FODC scheme, the new value can be calculated based on the computed value according to

$$\varphi_{new} = \varphi_{computed} - \beta_{FODC}\varphi_{FODC} \tag{16}$$

where φ stands for either the free surface elevation η or the velocity potential ϕ at the free surface; β_{FODC} is a case dependent correction coefficient,

typically ranging from 0.1 to 0.3, which takes the value of 0.2 in present study. φ_{FODC} is the four-order damping correction variable estimated in the following manner:

$$\varphi_{FODC} = \sum_{i=1}^{n} \left(\varphi_{i,SODC}^{D} - \varphi_{SODC}^{R} \right) W_i \tag{17}$$

$$\varphi_{SODC}^{R} = \sum_{i=1}^{n} \left(\varphi_{i,\ computed}^{D} - \varphi_{computed}^{R} \right) W_i \tag{18}$$

$$W_i = \frac{Dist_i}{\sum_{i=1}^{n} Dist_i} \tag{19}$$

where the superscripts R and D indicate the values of the receptor and the donor (see Figure 4 for details), respectively; i is the neighbouring donor index; n is the number of the neighbouring donors; φ_{SODC} is the second-order damping correction variable; W_i is the weight function in terms of the distance; $Dist$ is the distance between the receptor and each donor. The second-order damping correction variable φ_{SODC} is calculated on the face vertices (Figure 4a) and face centres (Figure 4b) for η and ϕ, respectively, depending on different storage locations. The main concepts in Eq. 18 for η and ϕ are identical that φ_{SODC}^{R} is estimated from the difference of computed φ between the donor and the receptor, weighted by their distance in Eq. 19. After that, Eq. 17 is applied to obtain φ_{FODC} from the weighted difference of φ_{SODC} between the donor and the receptor. The last step of the FODC scheme is to correct the computed value in the kinematic and dynamic free surface boundary conditions at the receptor according to Eq. 16 to obtain the final new value.

4. Validations and applications

In order to validate the proposed fully nonlinear numerical model, several representative test cases are selected here. In the first test case, the relaxation zone and a sponge layer for wave generation and absorption, respectively, are introduced in a 3-D numerical wave flume and the results are compared with the analytical solutions (Le Méhauté, 1976; Fenton, 1985), along with a mesh sensitivity study. In addition to wave propagation over a flat seabed, two more test cases involving wave propagation and transformation over a submerged bar are simulated and compared with experimental data and other

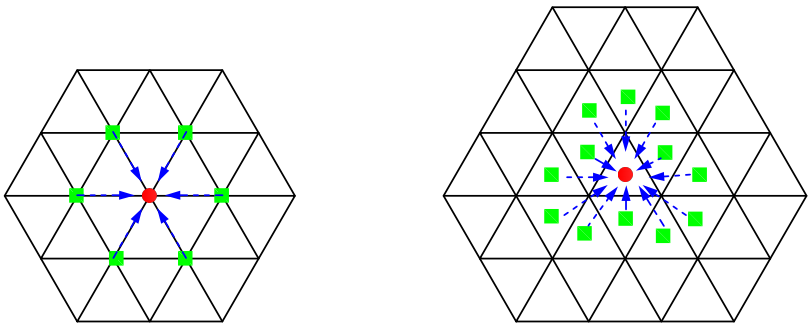

(a) Point fields (b) Face centre fields

Figure 4: Sketch of fourth-order damping correction. Red dot: Receptor; Green rectangular: Neighbouring donor.

existing numerical results. Furthermore, the validations of the code with 3-D shoaling cases are performed to evaluate its applicability of proposed FNPF model for modelling 3-D wave propagation and transformation. Finally, the proposed fully nonlinear potential flow model is validated against the experimental data and the numerical results from a NS-VoF model for the test cases of regular waves interaction with a bottom-mounted circular cylinder.

4.1. Wave generation and absorption

In this test case, wave generation and propagation in a 3-D wave tank is simulated, in which the relaxation zone near the inlet and a sponge layer near the outlet as shown in Figure 5 are introduced in the FNPF model to generate and absorb progressive waves. The case R2 and case R3 in Table 1, which are a second-order Stokes wave and a fifth-order Stokes wave, respectively, are selected to show the performance of the developed numerical model. In section 4.4, wave conditions cases R1 and R2 described in Table 1 will also be used for modelling wave-cylinder interactions. The lengths of the relaxation zone and sponge layer are set to one wavelength. The total length of the numerical wave tank is four times the wavelength in order to examine the capacity of wave absorption and reduce computational efforts. The mesh setup is also presented in Figure 5, where the mesh is refined in the vertical direction near free surface. To examine the mesh convergence of the solution, four different mesh setups are selected as listed in Table 2.

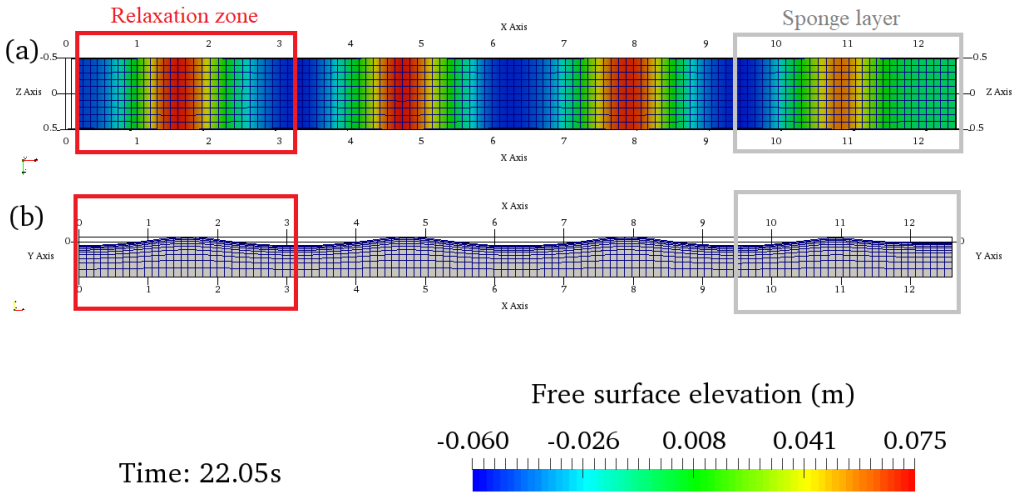

Figure 5: Snapshots of 3-D numerical wave flume. (a) Top view; (b) Side view.

Table 1: Wave parameters for wave generation in a 3-D wave flume

Case ID	Wave amplitude: A (m)	Wave height: H (m)	Wave period: T (s)	Water depth: d (m)	Wave length: λ (m)
R1	0.07	0.14	1.22	0.505	2.106
R2	0.06	0.12	1.63	0.505	3.164
R3	0.125	0.25	2	0.7	4.62

To measure the free surface elevation, two Wave Gauges (WGs) are located at $x = 0.05$m (WG1) and $x = 6$m (WG2), respectively. WG1 is used to measure the reproduction of analytical waves in the relaxation zone, while WG2 is adopted to measure the numerical waves in the working area. The simulation time is 40s, which is approximately 25 wave periods. In Figure 6, the numerical results at WG2 with four different mesh setups are shown and compared with analytical solution. It is evidently noticed that the wave amplitude with Mesh setup M1 dissipates gradually along the wave tank due to its coarseness and the numerical error introduced by the second-order finite volume scheme. As the cell number Per Wave Length (PWL) increases from 15 to 30, the simulated waves at WG2 become steady and closer to analytical solution. It can be seen that the difference in the numerical results between the mesh setups of M3 and M4 in the zoomed-in (Figure 6b-c) is negligible and they are all in good agreement with analytical solution. Therefore, based

Table 2: Meshes for sensitivity study

Mesh	Mesh setup (x, y, z)	Cells PWL	Total mesh number
M1	60×10×10	15	6,000
M2	80×10×10	20	8,000
M3	100×10×10	25	10,000
M4	120×10×10	30	12,000
M5	1080×30×5	50	162,000

Note: PWL is Per Wave Length.

on the mesh sensitivity study it is recommended to have over 25 cells PWL to maintain the stability and accuracy of progressive waves in the proposed FNPF numerical wave tank.

To show the capability of the current model to generate highly nonlinear waves, the fifth-order Stokes waves have been reproduced in the NWT using the proposed FNPF model. The size of a NWT for case R3 is 100m×0.7m×1m in x, y, and z directions, respectively, and the corresponding mesh setup M5 is listed in Table 2. Due to the high nonlinearity of the fifth-order Stokes waves, the number of cells PWL is slightly more than the recommended value above. The numerical results of case R3 are shown in Figure 7, where x is the distance away from inlet boundary. Excellent agreements have been achieved compared to analytical solution of fifth-order Stokes waves based on Fenton (1985), even at WG4 which is 30m away from wave generation zone. This indicates that the present FNPF model is capable of accurately predicting propagation of highly nonlinear waves in a NWT.

Table 3: Wave parameters for 2-D and 3-D shoaling

Case ID	Wave amplitude: A (m)	Wave height: H (m)	Wave period: T (s)	Water depth: d (m)	Wave length: λ (m)
2-D_S1	0.01	0.02	2.02	0.4	3.737
2-D_S2	0.018	0.036	1	0.4	1.4637
3-D_S1	0.0195	0.039	1	0.4572	1.4957
3-D_S2	0.0075	0.015	2	0.4572	3.9095
3-D_S3	0.0106	0.0212	2	0.4572	3.9095
3-D_S4	0.0068	0.0136	3	0.4572	6.1364

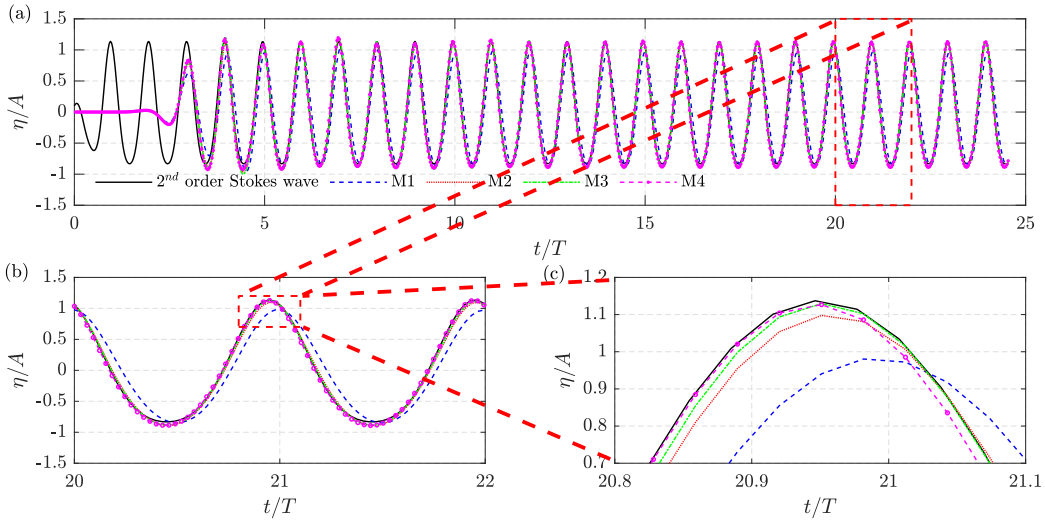

Figure 6: Time histories of free surface elevation at WG1 (analytical solution) and WG2 with various mesh densities. (a) Overall time history of free surface elevation; (b) Time history of free surface elevation within t/T = 20-22; (c) Time history of free surface elevation within t/T = 20.8-21.1 and η/A= 0.7-1.2.

4.2. 2-D shoaling

In this section, two more complex validation cases, i.e., a 2-D shoaling over a submerged slope with two different wave steepness, are performed to demonstrate the model's ability to accurately predict the effects of bathymetry on wave propagation and transformation. The wave parameters for these two shoaling cases are listed in Table 3, where the case IDs start with 2-D. The experiments of these 2-D cases are described in Beji and Battjes (1993, 1994). The corresponding mesh setups are tabulated in Table 4 and the mesh is refined horizontally in the area around the slope where the wave shoaling phenomenon is significant.

For the 2-D shoaling case, the sketch for laboratory setup is presented in Figure 8, and the time histories of wave elevation at different wave gauges obtained with mesh setup 2-D_M1 are shown in Figure 9. The CPU time taken for the simulation is 1141s using 3 processors (CPU: Intel® Xeon® CPU-E5 2699 v4 @ 2.20 GHz). It can be seen from Figure 9(a) that the incoming waves agree well with the experimental data, even after 10 wave periods. This indicates the target waves are well reproduced, which are also well absorbed by the relaxation zone and the sponge layer at the two ends of

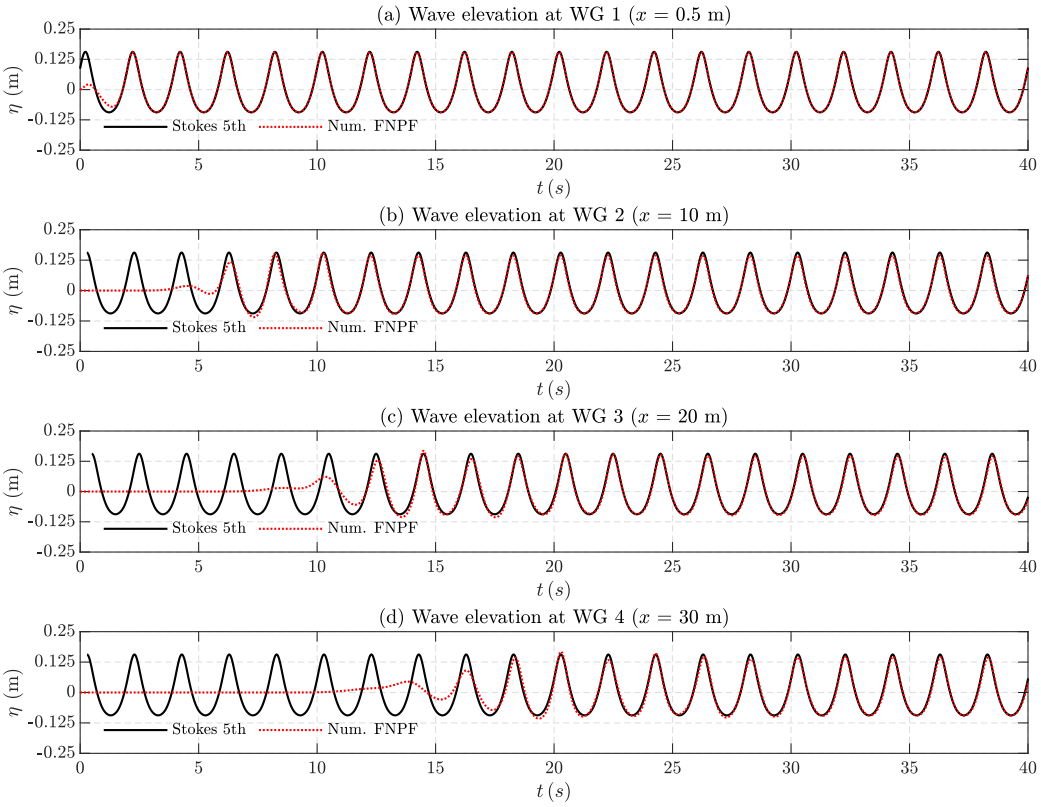

Figure 7: Time histories of free surface elevation at various WGs along the NWT. (a) WG1: $x = 0.5$m; (b) WG2: $x = 10$m; (c) WG3: $x = 20$m; (d) WG4: $x = 30$m.

the wave tank. According to the results at WG2 ($x = 12.5$m) to WG9 ($x = 21.0$m) Figure 9(b-h), decreasing water depth over the submerged slope leads to an increase of wave amplitude and stronger nonlinear effects, which can be observed from both the numerical and experimental results. The fairly good agreements between the numerical and experimental results clearly indicate the proposed FNPF model is able to accurately reproduce the 2-D wave shoaling process, including wave propagation and transformation, although a slight discrepancy between the numerical and experimental results can be observed at WGs 5-8 in Figure 9(e-h), presumably due to the coarse mesh used in the calculation.

To further examine the applicability of the proposed FNPF model in capturing higher nonlinear effects, a higher steepness wave (2-D_S2 in Table 3)

Table 4: Mesh for 2-D and 3-D shoaling

Case ID	Mesh setup (x, y, z)	Cells PWL	Total mesh number	Mesh size in x direction	Mesh size in y direction	Mesh size in z direction
2-D_M1	1213×25×1	Varied	30,325	7.7mm $< \Delta x <$ 210mm	5mm $< \Delta y <$31mm	N/A
2-D_M2	3000×20×1	Varied	60,000	4.4mm $< \Delta x <$ 210mm	3mm $< \Delta y <$61mm	N/A
3-D	1500×30×50	Varied	2,250,000	22.5mm $< \Delta x <$192mm	0.67mm $< \Delta y <$67.7mm	Δz = 121.92mm

Note: PWL is Per Wave Length.

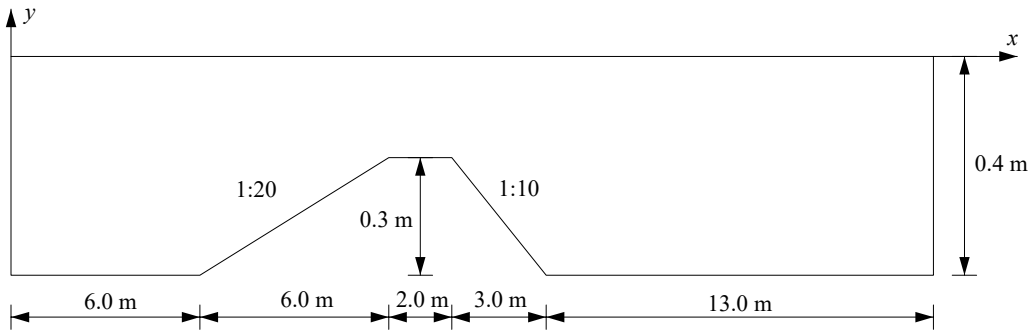

Figure 8: Sketch of numerical wave tank for the 2-D shoaling test case (not to scale).

is adopted to investigate the shoaling process over the same submerged bar in Figure 8. The total CPU time taken for the simulation is 4958s using 3 processors. This longer computational time may be attributed to the combined effects of larger velocities in the flow field and corresponding smaller time step under the same CFL number, and slightly increased cell numbers (2-D_M2 in Table 4). It should be noted that the original input wave height for the 2-D_S2 case was 0.041m as indicated in Beji and Battjes (1993), however, the experimental measurement of WG1, located at $x = 6.0$m just before the submerged slope, showed the generated wave height is actually around 0.036m. Therefore, this measured wave parameter ($H = 0.036$m) is adopted to reproduce the incident wave, instead of using the original wave height.

In Figure 10(a), the time history of free surface elevation at WG1($x =$ 6.0m) is compared with the experimental results, which demonstrates that the incident waves used in the wave tank test have been accurately repro-

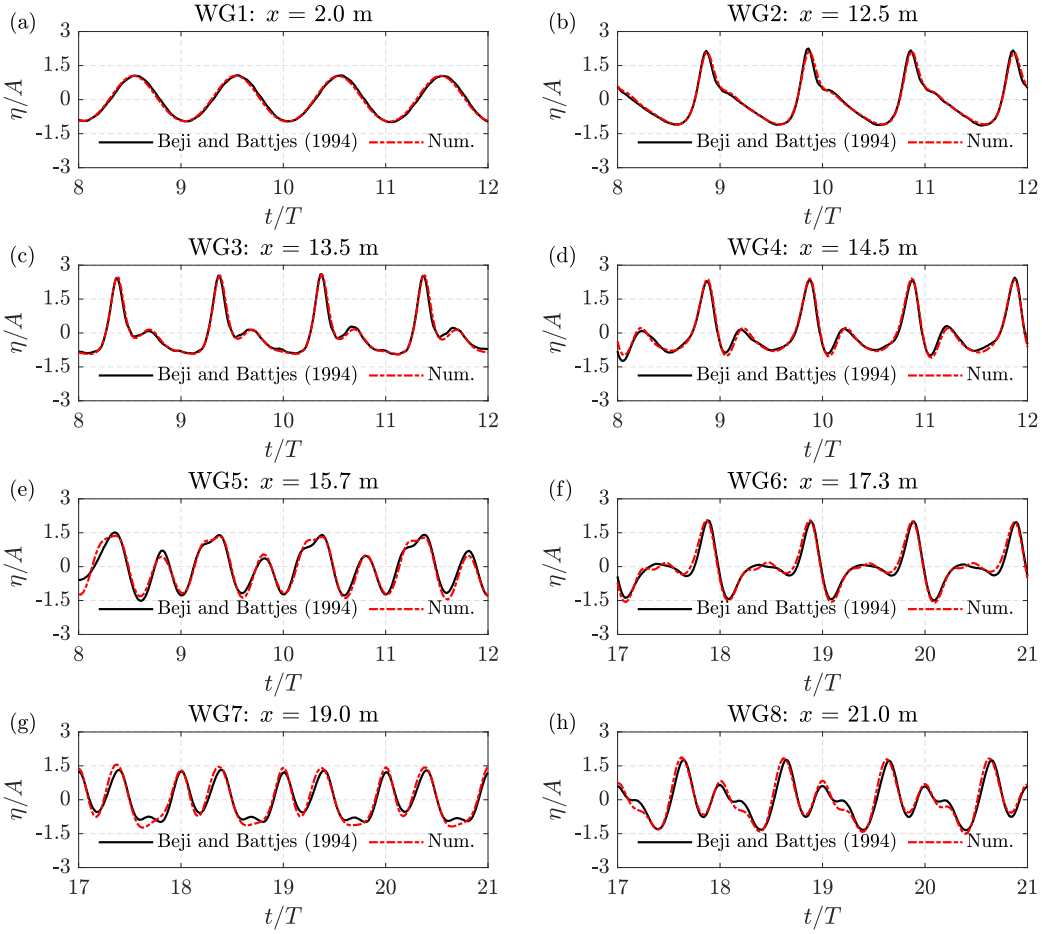

Figure 9: Free surface elevation at various locations and comparison with experimental data of case 2-D_S1 with mesh setup 2-D_M1.

duced by the numerical model. Furthermore, excellent agreements between numerical and experimental results are achieved at other positions as shown in Figure 10(b-d) when shoaling occurs and in Figure 10(e-f) when the wave is passing the rear slope. It can be concluded from the two validation cases that the proposed FNPF model is capable of accurately predicting wave propagation and transformation, though computationally it is more expensive than the high-order discretisation methods (Engsig-Karup et al., 2009; Ducrozet et al., 2014; Engsig-Karup et al., 2016), primarily due to the higher number of cells required for each wavelength and MEL method used in present FNPF model.

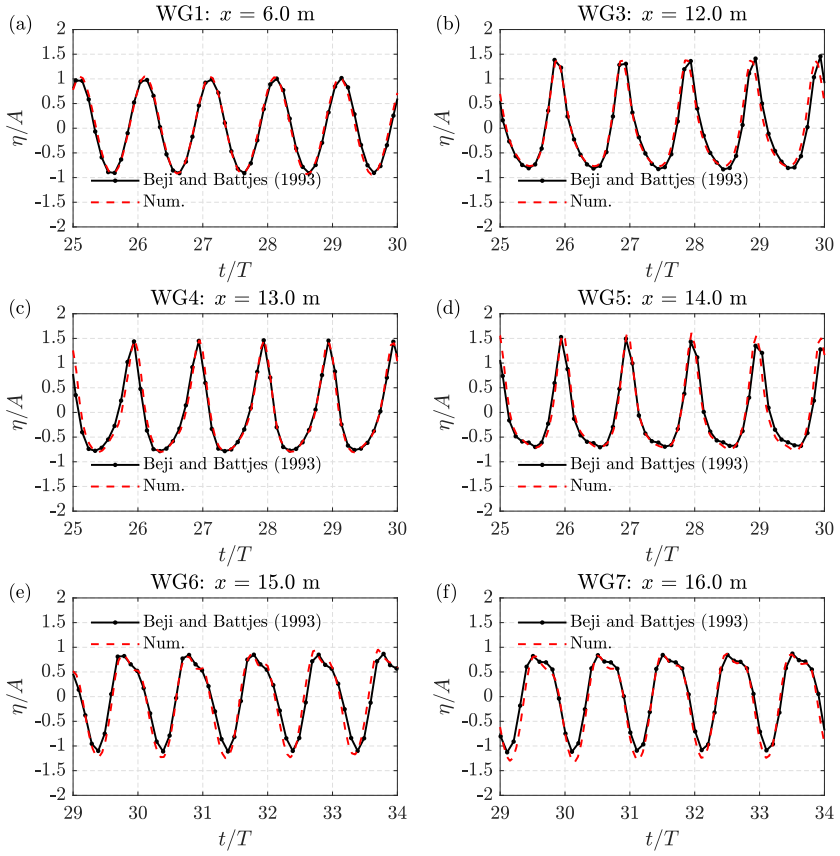

Figure 10: Free surface elevation at various locations and comparison with experimental data of case 2-D_S2 with mesh setup 2-D_M2

4.3. 3-D shoaling

In additional to the 2-D shoaling, the proposed FNPF model is applied to simulate the well-known benchmark test case of 3-D shoaling (Whalin, 1971) over a submerged semi-circular slope to demonstrate the capacity of the present fully nonlinear numerical model in predicting the nonlinear characteristics of 3-D wave propagation and transformation. In the 3-D shoaling experiment, the water depth is defined as follows: (1) the water depth at left flat bottom is 0.4572m with $0 \leq x \leq 10.67 - G(z)$, where $G(z) = \sqrt{z\,(6.096 - z)}$; (2) the water depth at semi-circular slope is described as $0.4572 + \frac{1}{25}\,(10.67 - G\,(z) - x)$ at $10.67 - G\,(z) < x < 18.29 - G\,(z)$; (3) the water depth at right flat bottom is 0.1524m with $18.29 - G\,(z) \leq x \leq 35.0$. Four different wave parameters are adopted, as listed in Table 3, while the

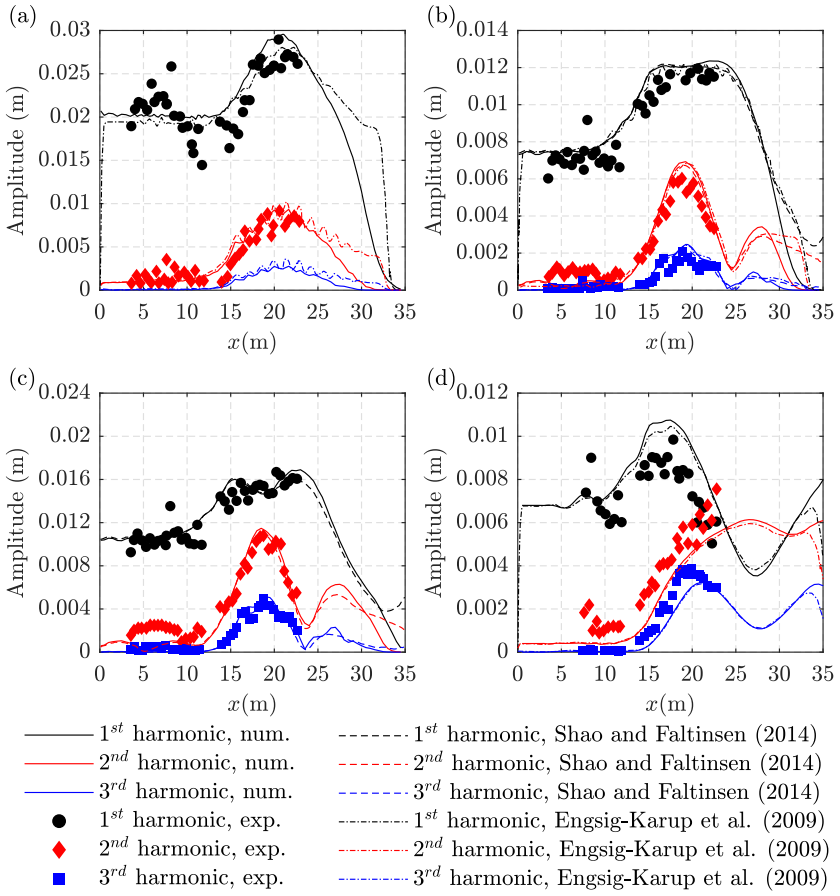

Figure 11: Harmonic components of numerical results and experimental measurements at the streamwise central line of numerical wave tank. (a) Case 3-D_S1; (b) Case 3-D_S2; (c) 3-D_S3; (d) 3-D_S4.

mesh setups are tabulated in Table 4 with various horizontal stretching ratios depending on the wavelength and wave focusing zone.

In Figure 11, the different harmonic components obtained by Fast Fourier Transform (FFT) along the streamwise central line of the domain are compared among the experimental measurements and the numerical results from the present FNPF model, Shao and Faltinsen (2014), and Engsig-Karup et al. (2009). Overall, the present numerical results agree well with the experimental results and other numerical results up to the third harmonic component for all the four different cases. The snapshots of Case 3-D_S3 in the form

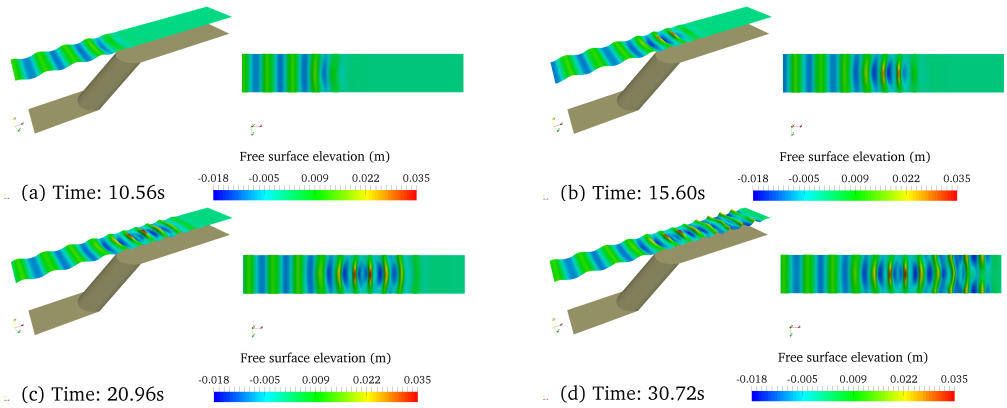

Figure 12: Snapshots of wave shoaling over a semi-circular slope for Case 3-D_S3 (Not in scale in the y direction and exaggerated 20 times)

of free surface elevation are presented in Figure 12, which shows that the 2-D waves generated in the relaxation zone first propagate towards the semi-circular slope (Figure 12a), then become locally steeper due to the presence of the semi-circular slope and eventually dissipated in the sponge layer zone (Figure 12b-d). From the above discussion, it is concluded that the 3-D and nonlinear wave effects of the flow problem can be accurately captured by the proposed FNPF model.

In addition to validating the FNPF model, the OpenMPI has been implemented for running the code in parallel with its efficiency evaluated using case 3-D_S4 shown in Table 3 and mesh setup 3-D in Table 4. The results showed that a speedup of 2.1 and 8.1 has been achieved from using 4 processors and 24 processors respectively, compared to the serial computation. As the focus of the current work was to develop and properly validate the 3D FNPF free surface code, there is still scope for further improving its parallel efficiency and this will be done in the near future.

4.4. Wave-cylinder interaction

To investigate the capability and accuracy of the present model in predicting wave loading on structures, a further test case involving wave interaction with a surface piercing cylinder is performed (Zang et al., 2010), together with an examination on the performance of the applied unstructured mesh for the relatively complex geometry of the computational domain. The setup of the unstructured mesh for the simulation is shown in Figure 13, where

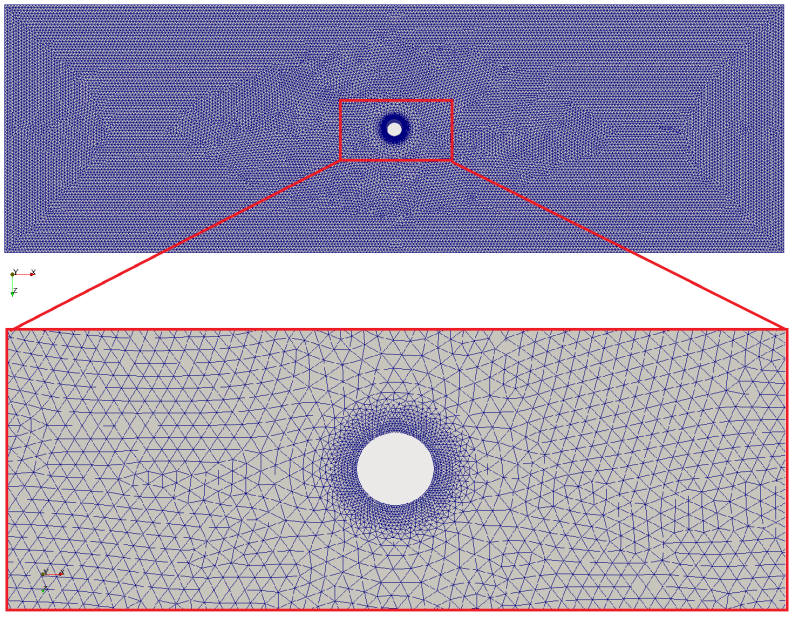

Figure 13: Mesh setup for wave-cylinder interaction.

nearly equal sized mesh cells are predominantly adopted in the computational domain, with local mesh refinement in the vicinity of the circular cylinder in order to capture the fine details of the wave-structure interaction. The ranges of mesh cell dimensions are 0.0075m $< \Delta x <$ 0.05m, 0.006m $< \Delta y <$ 0.0345m, 0.0075m $< \Delta z <$ 0.05m, respectively, and the total number of cells is around 1.4 million. The wave tank is 12.6m long, 4m wide, and 0.505 deep, in which the cylinder diameter is 0.25m. The relaxation zone for wave generation is 1 wavelength long and the length of sponge layer is two wavelengths.

Two sets of wave parameters in Chen et al. (2014) are adopted for validation as listed in Table 1. The FFT analysis in Chen et al. (2014) indicated that these two waves are second-order stokes waves and higher harmonic components are introduced when the incident wave interacts with the circular cylinder. These provide good validation test cases for the present FNPF model to examine its ability to model strongly nonlinear wave-wave and wave-structure interaction problems. In addition to the comparison with experimental measurements, the numerical results from a NS-VoF model are

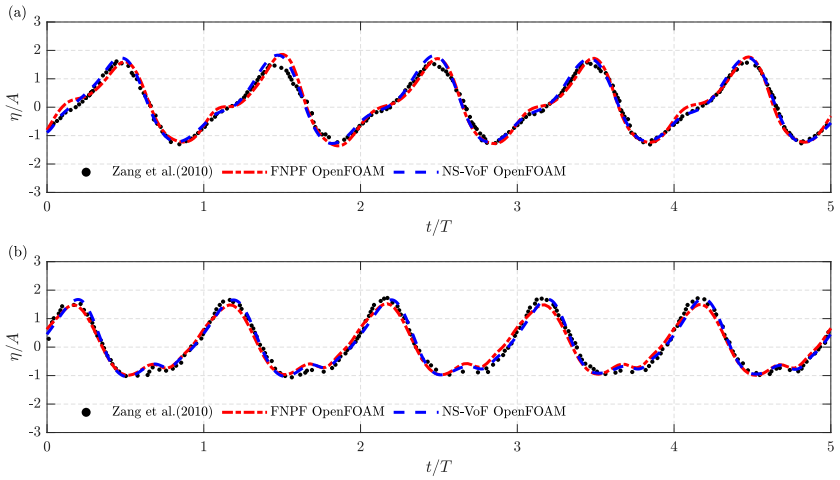

Figure 14: Free surface elevation at the front stagnation point of the cylinder. (a) Case R1; (b) Case R2.

also presented and compared with the results from the FNPF model in Figures 14 and 15 for the wave elevation and wave force, respectively. The fairly good agreements between the two numerical results and experimental data demonstrate that the present FNPF model has the capacity of capturing strongly nonlinear wave-cylinder interaction using the unstructured mesh setup, despite the small discrepancy of free surface elevation between the FNPF and NS-VoF models at wave troughs and wave crests as shown in Figure 14(a). This may be attributed to the existence of higher-order nonlinear components, which may appear in some local areas and be caused by the viscous effects. However, it can be observed from Figure 15 that the viscous effect plays an insignificant role in determining the inline force for these cases.

To clearly illustrate the interactions between the waves and a circular cylinder using the present FNPF model, the snapshots of free surface elevation of Case R1 within one wave period are shown in Figure 16, together with the mesh motions on cylinder surface. When the wave crest approaches the cylinder (Figure 16a-b), wave run-up takes place as indicated by the mesh movement on cylinder surface. After the passing of wave crest (Figure 16c), two wave fronts merge at the rear side of the cylinder, causing a large vertical motion of the surface mesh. Following this, the wave trough approaches the front stagnation point of the cylinder and a return flow from the rear side to the front side is evidently captured in Figure 16(d-e). Before the arrival of

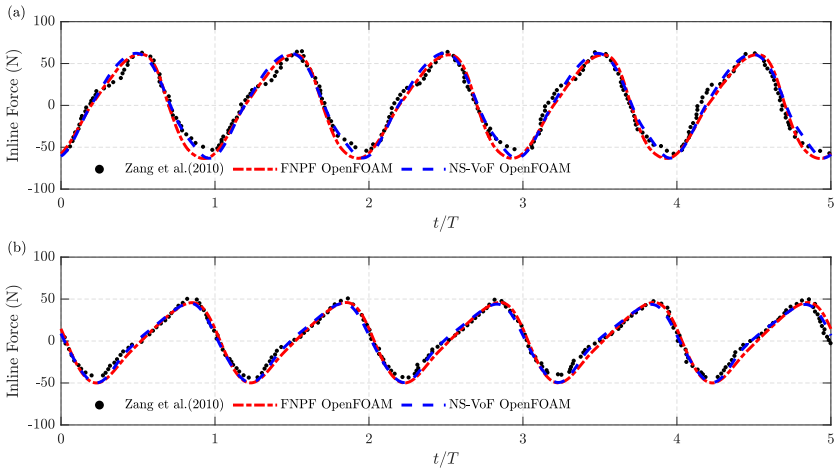

Figure 15: Time series of inline forces on the cylinder. (a) Case R1; (b) Case R2.

next wave crest at the front stagnation point, the return flow merges into a small wave run-up in Figure 16(f). Based on the results, it can be concluded that the present FNPF model is able to accurately capture the detailed flow patterns of the wave-structure interaction problem where the viscous effect is shown to be insignificant.

5. Conclusion

In this paper, a new fully nonlinear potential flow based numerical wave model is developed using Finite Volume Method on the platform of OpenFOAM, which provides an effective alternative for modelling wave-wave and wave-structure interaction problems and for coupling with the finite volume based Navier-Stokes models in OpenFOAM in a consistent and efficient manner. The development of the numerical model conforms to the coding standard of OpenFOAM and makes full use of the its existing functionalities. The numerical implementation of the present FNPF model is described in detail, which includes the variable interpolations between the cell centres and the cell faces/vertices for implementing the free surface boundary conditions, as well as the high-order smoothing technique for mitigating the issue of numerical instability. A variety of test cases have been simulated to validate the developed code and to demonstrate its robustness. Fairly good agreements between the present numerical results and the experimental measurements and other numerical results are obtained for all the test cases, which indicate

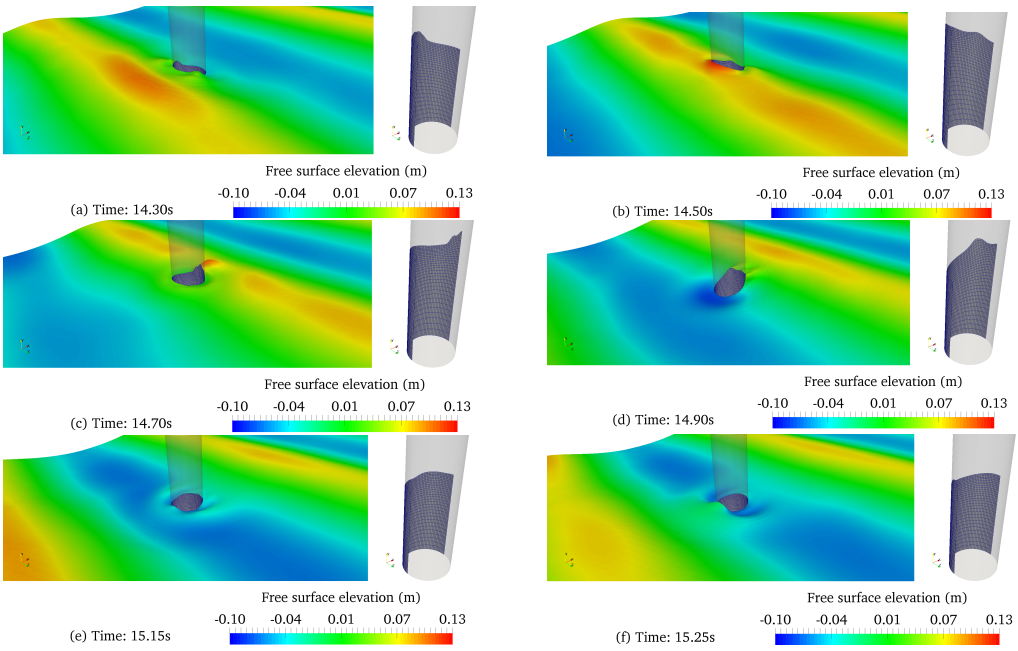

Figure 16: Snapshots of wave-cylinder interaction and mesh motions on cylinder surface for Case R1 at various time instants.

that the developed FNPF numerical model is able to accurately simulate the problems of wave generation, propagation and its interaction with fixed structures as long as no wave breaking occurs. One should be noted that, although the present FNPF model may be computationally more expensive than the existing high-order discretisation methods due to the requirements of finer mesh for spatial representation and MEL used to represent free surface, it is more flexible as far as the modelling of interaction between waves and floating structures with complex geometry is concerned. In the future, the model will be further optimised for better computational/parallel efficiency, extended to model the interactions between waves and floating structures, and coupled with the existing NS-VoF models in OpenFOAM to construct an efficient and robust numerical wave tank model.

Acknowledgements

This work is partially funded by the EPSRC (UK) projects 'A Zonal CFD Approach for Fully Nonlinear Simulations of Two Vessels in Launch and Recovery Operations' (EP/N008839/1), 'Extreme Loading on FOWT

under Complex Environmental Conditions' (EP/T004150/1), and 'A CCP on Wave/Structure Interaction: CCP-WSI' (EP/M022382). The first author would also like to acknowledge the funding from the Manchester Metropolitan University to sponsor a Research Fellowship position.

References

Amini-Afshar M, Bingham HB, Henshaw WD, Read R. A nonlinear potential-flow model for wave-structure interaction using high-order finite differences on overlapping grids. In: Preceeding of the 34th International Workshop on Water Waves and Floating Bodies (IWWWFB). .

Bai W, Eatock Taylor R. Higher-order boundary element simulation of fully nonlinear wave radiation by oscillating vertical cylinders. Applied Ocean Research 2006;28(4):247–65.

Bai W, Eatock Taylor R. Numerical simulation of fully nonlinear regular and focused wave diffraction around a vertical cylinder using domain decomposition. Applied Ocean Research 2007;29(1):55–71.

Bai W, Eatock Taylor R. Fully nonlinear simulation of wave interaction with fixed and floating flared structures. Ocean engineering 2009;36(3):223–36.

Bai W, Feng X, Eatock Taylor R, Ang K. Fully nonlinear analysis of near-trapping phenomenon around an array of cylinders. Applied Ocean Research 2014;44:71–81.

Beji S, Battjes J. Experimental investigation of wave propagation over a bar. Coastal Engineering 1993;19(1-2):151–62.

Beji S, Battjes J. Numerical simulation of nonlinear wave propagation over a bar. Coastal Engineering 1994;23(1-2):1–16.

Bingham HB, Zhang H. On the accuracy of finite-difference solutions for nonlinear water waves. Journal of Engineering Mathematics 2007;58(1-4):211–28.

Cai X, Langtangen HP, Nielsen BF, Tveito A. A finite element method for fully nonlinear water waves. Journal of Computational Physics 1998;143(2):544–68.

606 Celebl M, Kim M, Beck RF. Fully nonlinear 3-D numerical wave tank sim-
607 ulation. Journal of Ship Research 1998;42(1):33–45.

608 Chen H, Qian L, Bai W, Ma Z, Lin Z, Xue MA. Oblique focused wave
609 group generation and interaction with a fixed FPSO-shaped body: 3D
610 CFD simulations and comparison with experiments. Ocean Engineering
611 2019a;192:106524.

612 Chen H, Qian L, Ma Z, Bai W, Li Y, Causon D, Mingham C. Application
613 of an overset mesh based numerical wave tank for modelling realistic free-
614 surface hydrodynamic problems. Ocean Engineering 2019b;176:97–117.

615 Chen L, Zang J, Hillis A, Morgan G, Plummer A. Numerical investiga-
616 tion of wave–structure interaction using OpenFOAM. Ocean Engineering
617 2014;88:91–109.

618 Ducrozet G, Bonnefoy F, Le Touzé D, Ferrant P. Implementation and val-
619 idation of nonlinear wavemaker models in a HOS numerical wave tank.
620 International Journal of Offshore and Polar Engineering 2006;16(03).

621 Ducrozet G, Bonnefoy F, Le Touzé D, Ferrant P. HOS-ocean: Open-source
622 solver for nonlinear waves in open ocean based on high-order spectral
623 method. Computer Physics Communications 2016;203:245–54.

624 Ducrozet G, Engsig-Karup AP, Bingham HB, Ferrant P. A non-linear wave
625 decomposition model for efficient wave–structure interaction. Part A: For-
626 mulation, validations and analysis. Journal of Computational Physics
627 2014;257:863–83.

628 Eatock Taylor R, Wu G, Bai W, Hu Z. Numerical wave tanks based on finite
629 element and boundary element modeling. Journal of Offshore Mechanics
630 and Arctic Engineering 2008;130(3):031001.

631 Engsig-Karup AP. Unstructured nodal DG-FEM solution of high-order
632 Boussinesq-type equations. Ph.d.; 2007.

633 Engsig-Karup AP, Bingham HB, Lindberg O. An efficient flexible-order
634 model for 3D nonlinear water waves. Journal of computational physics
635 2009;228(6):2100–18.

Engsig-Karup AP, Eskilsson C. Spectral element FNPF simulation of focused wave groups impacting a fixed FPSO-type body. International Journal of Offshore and Polar Engineering 2019;29(02):141–8.

Engsig-Karup AP, Eskilsson C, Bigoni D. A stabilised nodal spectral element method for fully nonlinear water waves. Journal of Computational Physics 2016;318:1–21.

Engsig-Karup AP, Madsen MG, Glimberg SL. A massively parallel GPU-accelerated model for analysis of fully nonlinear free surface waves. International Journal for Numerical Methods in Fluids 2012;70(1):20–36.

Engsig-Karup AP, Monteserin C, Eskilsson C. A mixed eulerian–lagrangian spectral element method for nonlinear wave interaction with fixed structures. Water Waves 2019;1(2):315–42.

Fenton JD. A fifth-order stokes theory for steady waves. Journal of waterway, port, coastal, and ocean engineering 1985;111(2):216–34.

Ferrant P. Three-dimensional unsteady wave-body interactions by a Rankine boundary element method. Ship Technology Research 1993;40:165–75.

Fochesato C, Dias F. A fast method for nonlinear three-dimensional free-surface waves. Proceedings of the Royal Society A: Mathematical, Physical and Engineering Sciences 2006;462(2073):2715–35.

Grilli ST, Guyenne P, Dias F. A fully non-linear model for three-dimensional overturning waves over an arbitrary bottom. International Journal for Numerical Methods in Fluids 2001;35(7):829–67.

Grilli ST, Skourup J, Svendsen IA. An efficient boundary element method for nonlinear water waves. Engineering Analysis with Boundary Elements 1989;6(2):97–107.

Guignard S, Grilli ST, Marcer R, Rey V. Computation of shoaling and breaking waves in nearshore areas by the coupling of BEM and VOF methods. In: The Ninth International Offshore and Polar Engineering Conference. International Society of Offshore and Polar Engineers; 1999. .

Guyenne P, Grilli S. Numerical study of three-dimensional overturning waves in shallow water. Journal of Fluid Mechanics 2006;547:361–88.

667 Hannan M, Bai W. Nonlinear hydrodynamic responses of submerged mov-
668 ing payload in vicinity of a crane barge in waves. Marine Structures
669 2015;41:154–79.

670 Higuera P, Lara JL, Losada IJ. Realistic wave generation and active wave ab-
671 sorption for Navier–Stokes models: Application to OpenFOAM®. Coastal
672 Engineering 2013;71:102–18.

673 Higuera P, Losada IJ, Lara JL. Three-dimensional numerical wave generation
674 with moving boundaries. Coastal Engineering 2015;101:35–47.

675 Jacobsen NG, Fuhrman DR, Fredsøe J. A wave generation toolbox for the
676 open-source CFD library: OpenFoam®. International Journal for numer-
677 ical methods in fluids 2012;70(9):1073–88.

678 Le Méhauté B. An Introduction to Hydrodynamics and Water Waves. Spring
679 Study Ed. Springer, Berlin Heidelberg, Germany., 1976.

680 Lin Z, Guo Y, Jeng Ds, Liao C, Rey N. An integrated numerical model for
681 wave–soil–pipeline interactions. Coastal Engineering 2016;108:25–35.

682 Lin Z, Pokrajac D, Guo Y, Jeng DS, Tang T, Rey N, Zheng J, Zhang J.
683 Investigation of nonlinear wave-induced seabed response around mono-pile
684 foundation. Coastal Engineering 2017;121:197–211.

685 Lin Z, Pokrajac D, Guo Y, Liao C, Tang T. Near-trapping effect of wave-
686 cylinders interaction on pore water pressure and liquefaction around a
687 cylinder array. Ocean Engineering 2020;218:108047.

688 Lin Z, Qian L, Bai W, Ma Z, Chen H, Zhou J. Development of a 3D fully
689 nonlinear potential flow wave tank in framework of OpenFOAM. In: Pro-
690 ceedings of the ASME 38th International Conference on Ocean, Offshore
691 and Artic Engineering (OMAE). 2019. .

692 Ma Q, Wu G, Eatock Taylor R. Finite element simulation of fully non-linear
693 interaction between vertical cylinders and steep waves. Part 1: methodol-
694 ogy and numerical procedure. International Journal for Numerical Meth-
695 ods in Fluids 2001a;36(3):265–85.

696 Ma Q, Wu G, Eatock Taylor R. Finite element simulations of fully non-linear
697 interaction between vertical cylinders and steep waves. Part 2: numerical

results and validation. International Journal for Numerical Methods in Fluids 2001b;36(3):287–308.

Ma Q, Yan S. QALE-FEM for numerical modelling of non-linear interaction between 3d moored floating bodies and steep waves. International Journal for Numerical Methods in Engineering 2009;78(6):713–56.

Ma QW, Yan S. Quasi ALE finite element method for nonlinear water waves. Journal of computational physics 2006;212(1):52–72.

Martínez-Ferrer PJ, Qian L, Ma Z, Causon DM, Mingham CG. Improved numerical wave generation for modelling ocean and coastal engineering problems. Ocean Engineering 2018;152:257–72.

Mayer S, Garapon A, Sørensen LS. A fractional step method for unsteady free surface flow with applications to nonlinear wave dynamics. International Journal for Numerical Methods in Fluids 1998;28(2):293–315.

Mehmood A, Graham DI, Langfeld K, Greaves DM. OpenFOAM finite volume method implementation of a fully nonlinear potential flow model for simulating wave-structure interactions. In: The 25th International Ocean and Polar Engineering Conference. International Society of Offshore and Polar Engineers; 2015. .

Mehmood A, Graham DI, Langfeld K, Greaves DM. Numerical simulation of nonlinear water waves based on fully nonlinear potential flow theory in OpenFOAM®-Extend. In: The 26th International Ocean and Polar Engineering Conference. International Society of Offshore and Polar Engineers; 2016. .

Ning DZ, Shi J, Zou QP, Teng B. Investigation of hydrodynamic performance of an OWC (oscillating water column) wave energy device using a fully nonlinear HOBEM (higher-order boundary element method). Energy 2015;83:177–88.

Paulsen BT, Bredmose H, Bingham HB. An efficient domain decomposition strategy for wave loads on surface piercing circular cylinders. Coastal Engineering 2014a;86:57–76.

728 Paulsen BT, Bredmose H, Bingham HB, Jacobsen NG. Forcing of a bottom-
729 mounted circular cylinder by steep regular water waves at finite depth.
730 Journal of Fluid Mechanics 2014b;755:1–34.

731 Shao YL, Faltinsen OM. A harmonic polynomial cell (hpc) method for 3d
732 laplace equation with application in marine hydrodynamics. Journal of
733 Computational Physics 2014;274:312–32.

734 Song B, Zhang C. Boundary element study of wave impact on a vertical
735 wall with air entrapment. Engineering Analysis with Boundary Elements
736 2018;90:26–38.

737 Sriram V, Ma Q, Schlurmann T. A hybrid method for modelling two dimen-
738 sional non-breaking and breaking waves. Journal of computational physics
739 2014;272:429–54.

740 Turnbull MS, Borthwick AGL, Eatock Taylor R. Numerical wave tank based
741 on a σ-transformed finite element inviscid flow solver. International Journal
742 for Numerical Methods in Fluids 2003;42(6):641–63.

743 Wang J, Ma Q. Numerical techniques on improving computational efficiency
744 of spectral boundary integral method. International Journal for Numerical
745 Methods in Engineering 2015;102(10):1638–69.

746 Wang J, Ma Q, Yan S. A hybrid model for simulating rogue waves in random
747 seas on a large temporal and spatial scale. Journal of Computational
748 Physics 2016;313:279–309.

749 Whalin RW. The limit of applicability of linear wave refraction theory in a
750 convergence zone. Report; Research Report H-71-3, U.S. Army Corps of
751 Engineers, Waterways Experiment Station, Vicksburg, Mississippi; 1971.

752 Wu G, Eatock Taylor R. Finite element analysis of two-dimensional non-
753 linear transient water waves. Applied Ocean Research 1994;16(6):363–72.

754 Wu G, Ma Q, Eatock Taylor R. Numerical simulation of sloshing waves
755 in a 3D tank based on a finite element method. Applied ocean research
756 1998;20(6):337–55.

757 Yan S, Li Q, Wang J, Ma Q, Xie Z, Stoesser T. Comparative numerical
758 study on focusing wave interaction with fpso-like structure. International
759 Journal of Offshore and Polar Engineering 2019;29(02):149–57.

Yan S, Ma Q. Numerical simulation of fully nonlinear interaction between steep waves and 2d floating bodies using the QALE-FEM method. Journal of Computational physics 2007;221(2):666–92.

Yan S, Ma Q. Qale-fem for modelling 3d overturning waves. International Journal for Numerical Methods in Fluids 2010;63(6):743–68.

Zang J, Taylor PH, Morgan G, Orszaghova J, Grice J, Stringer R, Tello M. Steep wave and breaking wave impact on offshore wind turbine foundations–ringing re-visited. In: Proc. 25th International Workshop on Water Waves and Floating Bodies (IWWWFB). 2010. p. 1–4.